ACSNANO

www.acsnano.org

ARTICLE

Mixed-Dimensional Anti-ambipolar Phototransistors Based on 1D GaAsSb/2D MoS_2 Heterojunctions

Wei Wang, Weijun Wang, You Meng, Quan Quan, Zhengxun Lai, Dengji Li, Pengshan Xie, SenPo Yip, Xiaolin Kang, Xiuming Bu, Dong Chen, Chuntai Liu, and Johnny C. Ho*

Cite This: https://doi.org/10.1021/acsnano.2c03673

ABSTRACT: The incapability of modulating the photoresponse of assembled heterostructure devices has remained a challenge for the development of optoelectronics with multifunctionality. Here, a gate-tunable and anti-ambipolar phototransistor is reported based on 1D GaAsSb nanowire/2D MoS_2 nanoflake mixed-dimensional van der Waals heterojunctions. The resulting heterojunction shows apparently asymmetric control over the anti-ambipolar transfer characteristics, possessing potential to implement electronic functions in logic circuits. Meanwhile, such an anti-ambipolar device allows the synchronous adjustment of band slope and depletion regions by gating in both components, thereby giving rise to the gate-tunability of the photoresponse. Coupled with the synergistic effect of the materials in different dimensionality, the hybrid heterojunction can be readily modulated by the external gate to achieve a high-performance photodetector exhibiting a large on/off current ratio of 4×10^4, fast response of 50 μs, and high detectivity of 1.64×10^{11} Jones. Due to the formation of type-II band alignment and strong interfacial coupling, a prominent photovoltaic response is explored in the heterojunction as well. Finally, a visible image sensor based on this hybrid device is demonstrated with good imaging capability, suggesting the promising application prospect in future optoelectronic systems.

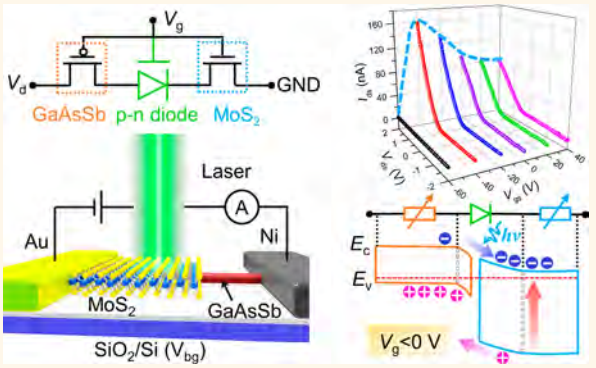

KEYWORDS: *heterojunction, anti-ambipolar, gate-tunable, phototransistor, image sensor*

In the past decade, a variety of dimensionally abrupt heterostructures have been realized on the basis of layered 2D semiconductors for their atomically smooth surface and pronounced electronic characteristics.[1−4] Particularly, the emergence of 2D van der Waals (vdW) heterostructures has expanded the possibility of diverse nanoscale functional devices through integrating disparate materials with artificially stacked architectures. These devices include light-emitting diodes,[5−7] nonvolatile memory cells,[8,9] Schottky junction devices,[10,11] complementary metal-oxide-semiconductor (CMOS) inverters,[12,13] and tunneling field-effect transistors.[14,15] The most prominent among these vdW nanodevices is the realization of anti-ambipolar transistors, with the first demonstration reported in carbon nanotube−MoS_2 p−n heterostructures[16] and more recently in various vdW heterojunctions, such as single-walled carbon nanotube (SWCNT)−amorphous indium gallium zinc oxide (α-IGZO),[17] pentacene−MoS_2,[18] WSe_2−WS_2,[19] SnO−MoS_2,[20] InSe−WSe_2,[21] and ReS_2−Te heterostructures.[22] The anti-ambipolar behavior can be deemed as deriving from the field-effect transistor (FET) channel composed of p-type and n-type semiconductors in series. It presents a convex shape transfer characteristic in which the channel electrical conductance peaks at a specific gate bias. This phenomenon is distinctly different from the transfer curves of unipolar FETs and regular ambipolar devices. In fact, this anti-ambipolar characteristic is quite advantageous to implement complicated electronic functions simply by using a single device in logic circuits, optoelectronics, and spiking neurons.[23,24] For instance, the transfer characteristics of these devices with the flipping of transconductance have revealed the utilization potentiality as three-terminal device units, including frequency doubling, binary phase shift keying, and ternary logic

Received: April 14, 2022
Accepted: June 20, 2022

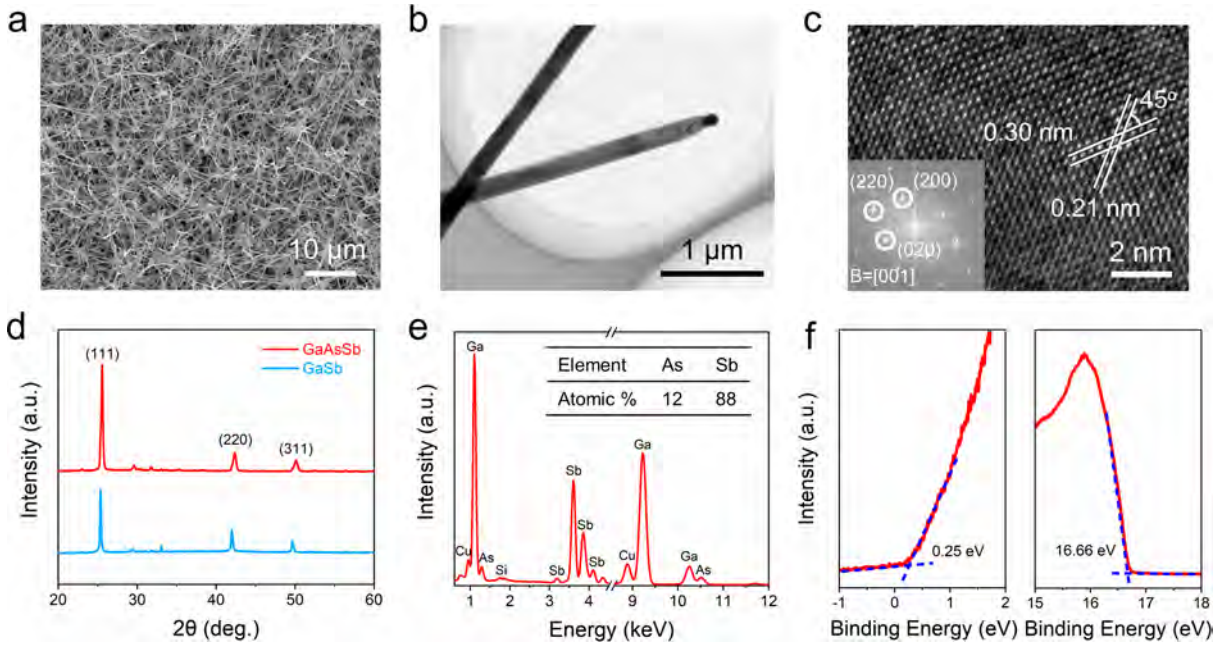

Figure 1. Morphology, phase composition, and UPS characterization of synthesized GaAsSb nanowires. (a) SEM and (b) TEM images of as-grown GaAsSb nanowires. (c) HRTEM image of the GaAsSb NW body. The inset shows the corresponding fast Fourier transform pattern. (d) XRD patterns of GaSb and GaAsSb nanowires synthesized by the solid-source CVD method. (e) EDS spectrum and the determination of the corresponding element composition of the GaAsSb NW body. (f) UPS spectrum of GaAsSb nanowires. The blue dashed lines mark the baselines and the tangents of the curves. The intersections of the tangents with the baselines indicate the edges of the UPS spectrum.

inverter, significantly reducing the number of circuit elements and thus simplifying the circuit design compared to conventional FET technologies.[17,25−27]

Apart from the aforementioned features, anti-ambipolar transistors based on lateral p−n heterojunctions also possess gate-tunable rectification characteristics, which can be used to develop gate-tunable rectifier circuits and photodiodes.[16,28,29] Since the anti-ambipolar devices enable both positive and negative transconductance, the p/n-type components can be readily modulated by a capacitively coupled gate bias. In this way, the charge transport of the constituent materials can be widely tuned from a nearly insulating state to a highly rectifying condition, which is subject to the degree of interfacial band bending caused by shifted Fermi levels. Therefore, the capability of altering the interfacial potential difference and the depletion width indicates that it is possible for such anti-ambipolar devices to manipulate the amplitude of a photocurrent to achieve a maximum in the gated heterostructures. Nevertheless, studies of photodetection on such nanodevice geometries with external gate modulation are still basically lacking. This may be due to the challenging fabrication of anti-ambipolar heterodiodes with reliable and exceptional performances. First, the turn-on voltages (V_{on}) and carrier densities of both p/n-type transistors should be precisely controlled. Specifically, the turn-on voltage of a p-type semiconductor needs to be larger than that of the n-type counterpart. Second, it requires the shrinking of the device dimensionality and the utilization of local gating. On one hand, scaling down the device dimensions and applying local gating are expected to enhance the anti-ambipolar frequency doubling performance and enable higher operating frequencies accordingly.[17] On the other hand, the shrinkage of the active region leads to reduced capacitance, thereby rendering the photodetectors intrinsically faster, more sensitive, and energy-efficient.[30−32] Last but not least, a high-quality and strongly coupled heterointerface is also crucial to produce an efficient charge transfer. In this regard, mixed-dimensional heterostructures consisting of 1D nanowires (NWs) and layered 2D materials offer an effective strategy for the design of multifunctional and high-performance anti-ambipolar optoelectronics. The reduced dimensionality of NWs can distinctly decrease the active region of the heterostructures. Meanwhile, owing to the wave-guiding effect, NWs as well play a functional role in light trapping to enhance light-to-current conversion efficiency substantially.[33] In terms of unique physical properties of 2D materials, the nature of the dangling-bond-free surface enables the formation of hybrid vdW heterostructures when integrated with materials with different dimensionality. The strong vdW coupling in such mixed-dimensional heterostructures can contribute to efficient photocarrier separation and transport under light exposure.[34]

In general, the synergistic effect in the mixed-dimensional heterostructures would bring great significance in constructing anti-ambipolar optoelectronics with diverse functionalities. However, there has still been rare demonstration of heterojunctions combining a p-type III−V nanowire and an n-type 2D semiconductor in such systems to our best knowledge. Herein, we develop a high-performance gate-tunable anti-ambipolar phototransistor based on 1D GaAsSb/2D MoS_2 heterojunctions. The multi-elemental feature of GaAsSb nanowires allows multiple degrees of freedom in controlling electronic properties by means of stoichiometric variation. Alloying with a certain amount of As composition, the GaAsSb nanowire can form a typical type-II band alignment with a MoS_2 nanoflake at the heterointerface. Also, the high intrinsic carrier mobility of both integrated constituents has a beneficial effect on shortening the carrier-transit time within the heterostructure device channel. With optimal gate modulation, the heterostructure photodiode delivers a respectable performance with an on/off current

https://doi.org/10.1021/acsnano.2c03673
ACS Nano XXXX, XXX, XXX−XXX

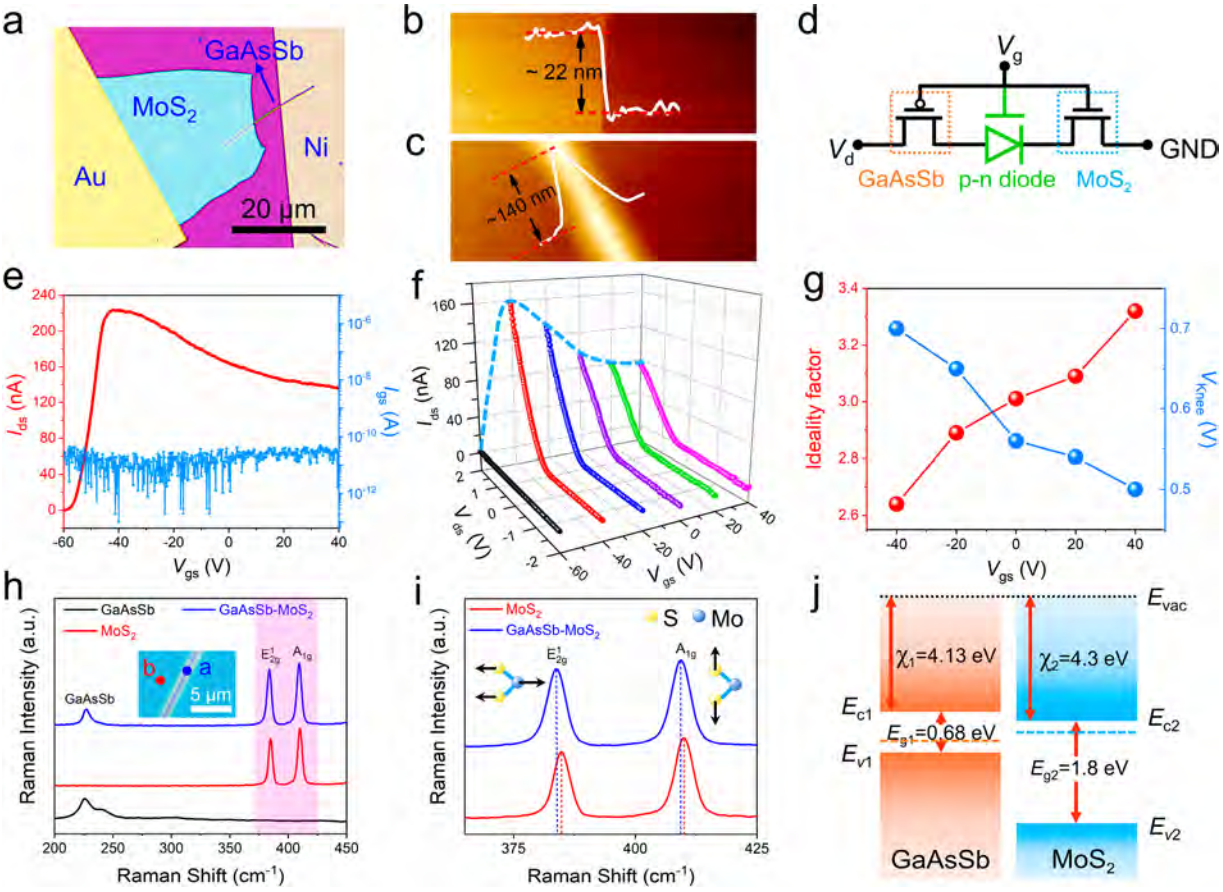

Figure 2. Electrical properties, Raman characterization, and band alignment of the GaAsSb/MoS_2 heterojunction. (a) Optical image of the 1D GaAsSb/2D MoS_2 heterostructure device. (b, c) AFM images of the MoS_2 nanosheet and the GaAsSb nanowire of the mixed-dimensional device, respectively, in panel (a). The height profiles indicate the MoS_2 layers and GaAsSb NWs are ~22 and ~140 nm in thickness, respectively. (d) Electrical configuration of the device, including the three parts represented in different colors. (e) Transfer characteristics and (f) output characteristics of the GaAsSb/MoS_2 heterostructure device. (g) Ideality factors and the knee voltage values extracted from the *I*–*V* curves in panel (f). (h) Raman spectra measured on the GaAsSb NW, MoS_2 nanosheet, and GaAsSb/MoS_2 p–n heterojunction. The inset shows the optical image of the heterostructure used for the Raman and PL characterization. (i) Comparison of the Raman spectra in the marked pink area of panel (h) in detail. (j) Energy band alignment of GaAsSb and MoS_2 before contact. χ_1, E_{g1}, and E_{g2} are determined from experimental results. χ_2 is extracted from related literature.

ratio of 4×10^4, a response time of 50 μs, and a detectivity of 1.64×10^{11} Jones under 532 nm illumination. Furthermore, the p–n heterojunction shows a photovoltaic response with an open-circuit voltage of ~0.2 V. More importantly, a visible image sensor is demonstrated by utilizing the heterojunction diode as a basic pixel unit. These unique characteristics of 1D GaAsSb/2D MoS_2 lateral p–n heterojunctions are expected to leverage further efforts in pursuing anti-ambipolar optoelectronic devices with multifunctionality using mixed-dimensional vdW heterostructures.

RESULTS AND DISCUSSION

In terms of modulating the electronic and optoelectronic properties, ternary alloy nanowires offer an advantage over elemental or binary semiconductor nanowires. As far as GaAsSb nanowires are concerned, Sb alloying at high content can tremendously increase the carrier concentration and thus improve the typical drawback of low hole mobility of pristine GaAs nanowires.[35,36] In turn, the adverse nonradiative carrier recombination would be diminished with the As composition introduced into GaSb NWs.[37,38] In this work, the ternary GaAsSb nanowires were synthesized *via* a Au-catalyzed solid-source chemical vapor deposition (SS-CVD) method as reported elsewhere.[39,40] As shown in the scanning electron microscope (SEM) image (Figure 1a), the obtained GaAsSb NWs are grown uniformly on amorphous SiO_2/Si substrates with a high growth density and an average length of over 20 μm. Based on the corresponding transmission electron microscope (TEM) image (Figure 1b), the NWs present a smooth surface morphology without distinct parasitic islands on the side facets. The high-resolution transmission electron microscopy (HRTEM) indicates the clear lattice fringes with interplanar distances of 0.21 and 0.30 nm (Figure 1c), which corresponds to the spacing along {110} planes and {100} planes of GaAsSb NWs, respectively. The figure inset shows the corresponding fast Fourier transform (FFT) pattern, demonstrating the single-crystalline zinc blende structure of NWs. The pure zinc blende crystal structure without any wurtzite phase can further be verified for the GaAsSb NWs by X-ray diffraction (XRD) patterns, as shown in Figure 1d. As compared with GaSb nanowires, the main peaks of GaAsSb NWs are found to shift toward the larger angle with As alloying, elucidating the decreased lattice parameter due to the smaller size of As atoms substituting the Sb atoms. These phase-pure NWs with low defect concentrations suggest good

https://doi.org/10.1021/acsnano.2c03673
ACS Nano XXXX, XXX, XXX–XXX

crystal quality, which would lead to reduced carrier scattering, which is essential for the subsequent application in hybrid heterojunctions. Moreover, energy dispersive X-ray spectroscopy (EDS) was employed to determine the chemical composition (Figure 1e), which is found to be $GaAs_{0.12}Sb_{0.88}$ from the statistics of more than 20 NWs.

For the sake of configuration into heterojunctions, it is necessary to determine the energy band structure of GaAsSb nanowires by using Tauc plots and ultraviolet photoelectron spectra (UPS). The optical bandgap of NWs was investigated by UV−vis−NIR diffuse reflectance spectrum (DRS) as presented in Figure S1a. Based on the Tauc plot equation, namely, $(\alpha h\nu)^2 = A(h\nu - E_g)$, the bandgap value ($E_g$) of GaAsSb NWs is estimated to be 0.68 eV by measuring the *x*-axis intercept of an extrapolated line from the linear regime of the curve (Figure S1b, black dashed line). Aside from the bandgap, the work function and ionization potential (equivalent to the valence band energy E_v) were ascertained by the UPS spectrum as depicted in Figure 1f. According to the linear intersection method, the E_v value of GaAsSb NWs is calculated to be −4.81 eV (*vs* vacuum) through subtracting the width of the He I UPS spectrum from the excitation energy (21.22 eV). Correspondingly, the conduction band value (E_c) is thus −4.13 eV from the formula $E_c = E_v + E_g$. Meanwhile, the work function (−4.56 eV) of GaAsSb NWs can be determined by adding E_v to the second electron cutoff energy. From the above results, the energy band structure of as-grown GaAsSb NWs then can be well presented in Figure S1c.

The GaAsSb/MoS_2 heterojunction device was fabricated by stacking a MoS_2 nanoflake above the GaAsSb NW through van der Waals integration on a SiO_2/Si substrate with 270 nm thick thermal grown oxide. To measure the electronic properties of the junction, Au and Ni were chosen to inject electrons and holes into the n-MoS_2 flake and p-GaAsSb NW, respectively.[18,36] The detailed fabrication process for the heterojunction can be found in Figure S2 and the Methods section. As shown in Figures S3 and S4, the individual GaAsSb and MoS_2 FETs exhibit respectively p-type and n-type channel characteristics due to the unintentional doping in the channel material. Based on the output curves, both GaAsSb and MoS_2 are well contacted with their electrodes, indicating that the Schottky barrier has little impact on the electrical performance of the heterojunction. Figure 2a illustrates an optical microscope image of a typical mixed-dimensional GaAsSb/MoS_2 heterojunction diode. The thicknesses of the mechanically exfoliated MoS_2 nanoflake and CVD-synthesized GaAsSb NW are about 22 nm (≈34 layers) and 140 nm, respectively, as confirmed by the atomic force microscope (AFM) in Figure 2b and c. The device configuration can be regarded as the combination of three functional parts in a series-resistance mode: an n-type MoS_2 FET, a GaAsSb/MoS_2 p−n diode, and a p-type GaAsSb FET (Figure 2d). A gate voltage (V_{gs}) applied to the SiO_2/Si substrate adjusts the carrier concentration in each semiconducting terminal. In this regard, this gated heterojunction construction has superiority over controlling the performance of the p−n heterojunction through electrostatic doping, while for the traditional Si/Ge-based diodes, the doping level is primarily constrained by diffusion or implantation of substitutional impurities, implying minimum control on the doping profile following device fabrication.

The electronic performance of the heterojunction device was also evaluated with the n-contact grounded. An obvious anti-ambipolar response can be observed from the transfer characteristics under a forward source−drain bias of 2 V (Figure 2e), demonstrating the gate-tunability of the current through the p−n heterojunction. The anti-ambipolar behaviors of additional devices with the same configuration can be found in Figure S5. Meanwhile, the gate leakage current (below 40 pA) is negligible as compared with the channel current. These unique transfer characteristics result from the FET channel comprising a p-type and an n-type semiconductor configured in series, in which the total current reaches a maximum when both transistors are turned on (near V_{gs} = −40 V) and declines to a minimum when either device is turned off (V_{gs} = −60 and 40 V). It is noted that this anti-ambipolar pattern is asymmetric with different transconductance on either side of the peak current. The asymmetric anti-ambipolarity in transfer plots has also been reported in other vdW p−n heterojunction systems.[19,20,41] Such hybrid devices have potential in building frequency doubling and binary phase shift keying units in the field of communications. The output curves can also demonstrate the gate tunability of the p−n junction as the gate bias varies from −60 to 40 V (Figure 2f). This way, the heterojunction transitions from a nearly insulating state at the negative extreme of the V_{gs} range to a highly rectifying output behavior at V_{gs} = −40 V, followed by the growing series resistance with further increasing gate bias. The rectification ratio can be tuned from 17 to 6×10^2 by the electrostatic doping of V_{gs} from −40 V to 40 V, among which the highest value is attained at a V_{gs} of −40 V (Figure S6). In this heterojunction, the utilization of the gate is then verified to have capability in tailoring the doping concentration of both semiconductors, thereby enabling tunability of the built-in voltage and rectifying behavior. Furthermore, based on the *I*−*V* plots, the gate dependence of the ideality factor and knee voltage (V_{knee}) are evaluated and compiled in Figure 2g. According to the slope of ln*I*−*V* plots (Figure S7a), the ideality factor values of the device can be derived from the following expression:

$$n = \frac{q}{k_B T}\frac{dV}{d\ln I} \quad (1)$$

where q is the elementary charge, k_B is Boltzmann's constant, and T is Kelvin temperature. With the increase in V_{gs}, the ideality factors witness a monoclinic ascending trend from 2.64 to 3.32, whereas a contrary tendency is observed for the knee voltage. The extracted V_{knee} of 0.7 V at V_{gs} = −40 V is almost equal to that of the conventional Si-based p−n junction.[42] Although the ideality factors exceed 2, they are still comparable to or even better than the reported SWCNT−MoS_2, GaAs−graphene, and ZnO−WSe_2 diodes.[16,43,44]

Here, the gate tunability of the anti-ambipolar transistor performance can be attributed to the high-quality heterointerface and the properly configured band alignment between GaAsSb and MoS_2. The coupling effect and charge transfer at the interface can be verified *via* the optical measurements. The Raman spectra collected from the GaAsSb nanowire, MoS_2 nanosheet, and overlapped heterojunction are exhibited in Figure 2h. The in-plane E^1_{2g} (384.8 cm^{-1}) and out-of-plane A_{1g} modes (410.2 cm^{-1}) are explicitly shown in the MoS_2 Raman spectrum measured from the red spot in the figure inset. The peak spacing of ∼25 cm^{-1} between E^1_{2g} and A_{1g} vibration modes indicates that the MoS_2 flake has four or more layers, which is in accordance with the AFM analysis as presented in Figure 2b.[45] It can be seen that the Raman signals from the overlapped heterostructure region (blue spot in the figure

https://doi.org/10.1021/acsnano.2c03673
ACS Nano XXXX, XXX, XXX−XXX

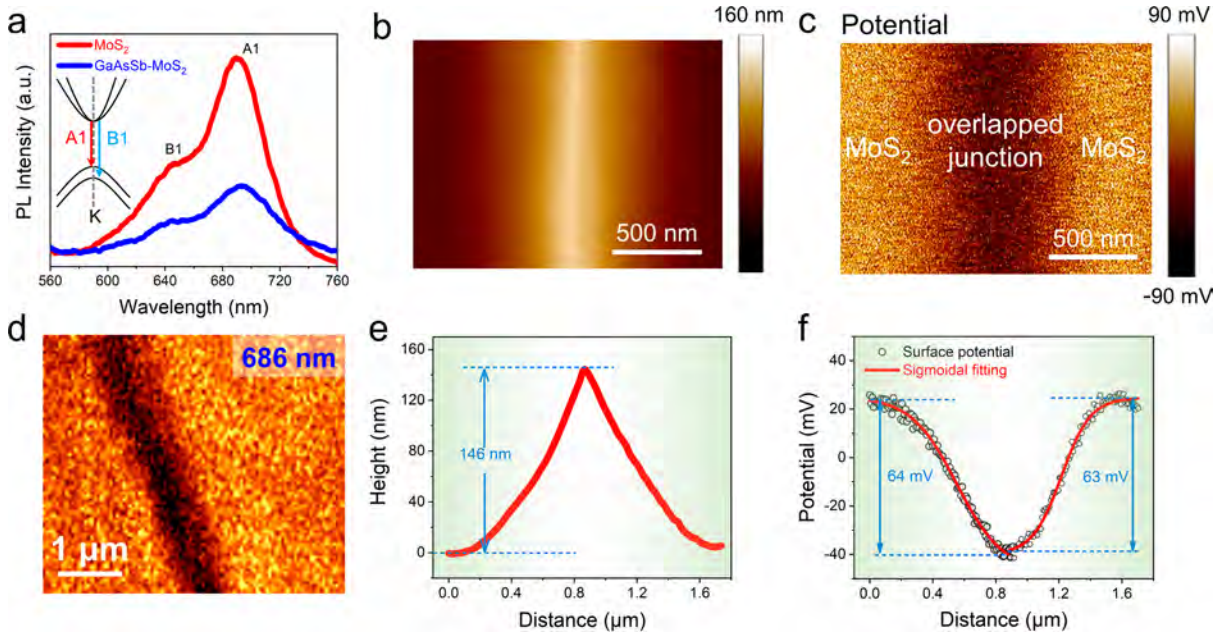

Figure 3. PL, AFM, and KPFM characterizations of the GaAsSb/MoS_2 heterojunction. (a) Photoluminescence spectra of MoS_2 and the GaAsSb/MoS_2 heterostructure. The schematic diagram demonstrates the direct transitions (A1 and B1 exciton) at the K point. (b) AFM topography and (c) the corresponding KPFM surface potential image of the GaAsSb/MoS_2 p−n heterojunction. (d) PL mapping measured at the wavelength of 686 nm on the GaAsSb/MoS_2 heterostructure. (e, f) Extracted height profile and surface potential across the MoS_2−junction−MoS_2 surface from panels (b) and (c), respectively.

inset) are the sum of the two individual signals obtained separately from the p-type GaAsSb and the n-type MoS_2, which confirms the formation of a vertically stacked p-GaAsSb and n-MoS_2 heterojunction. Compared with the individual MoS_2 displayed in Figure 2i, the E^1_{2g} and A_{1g} characteristic peaks in the overlapped MoS_2 regions are red-shifted, implying the charge transfer from GaAsSb to MoS_2 occurred at the interface.[46,47] Hence, strong interfacial coupling is confirmed in the vdW hybrid heterojunction. In addition, the energy band alignment of GaAsSb/MoS_2 is proposed in Figure 2j according to the established band structure of GaAsSb and related literature. The bandgap of MoS_2 is determined to be 1.8 eV from the subsequent photoluminescence (PL) test given in Figure 3a. The electron affinity and work function of multilayered MoS_2 are reported to be 4.3 and 4.5 eV.[48] Then, the offsets of the conduction band and valence band are approximately 0.17 and 1.29 eV, respectively. Therefore, a typical type II p−n heterostructure is formed, which is favorable to the electrical transmission and high-speed photoresponse. The potential difference (~60 mV) induced by the misaligned Fermi level at the heterointerface will be validated in a later section.

However, it is still insufficient and also controversial to demonstrate the high-quality heterointerface only by the Raman spectra analysis and the suggested band alignment. To further investigate the interlayer coupling effect at the GaAsSb/MoS_2 interface, we have conducted micro-PL measurement and Kelvin probe force microscopy (KPFM) scanning. The PL test was carried out using a 532 nm laser with a spot diameter of ~1 μm. As depicted in Figure 3a, the emission spectrum of the MoS_2 nanoflake (acquired at the red spot in Figure 2h inset) consists of one major peak and one minor peak at about 686 and 643 nm, respectively. These two resonances, known as A1 and B1 excitons, are from the direct excitonic transitions at the K point of the Brillouin zone, between which the energy difference is caused by the spin−orbital splitting of the valence band as shown in Figure 3a inset.[49,50] By contrast, the photoluminescence at the overlapped region is obviously quenched for both emission peaks (acquired at the blue spot in Figure 2h inset). The strong suppression of photoluminescence for the MoS_2 segment stacked on GaAsSb NW is also apparently demonstrated from the corresponding PL mapping image at a 686 nm wavelength (Figure 3d). In principle, the charge transfer will lead to increased nonradiative recombination and consequently the quenched light emission from all transitions. Accordingly, the observation of reduced photoluminescence from both A1 and B1 exciton resonances indicates the efficient separation of photogenerated carriers across the heterojunction, verifying the type II GaAsSb/MoS_2 band alignment formed at the interface.[51,52] To quantify the quenching effect of the heterojunction, we bring in the quenching factor, $Q = I_{MoS_2}/I_{GaAsSb/MoS_2}$.[53] Here, I_{MoS_2} is the intensity of the MoS_2 PL peak at 686 nm, and I_{GaAsSb/MoS_2} is the intensity of the same peak from the overlapped region. Therefore, the quenching factor of the GaAsSb/MoS_2 heterojunction is determined to be ~3 from the data shown in Figure 3a. Next, the AFM and KPFM characterizations were performed to investigate the corresponding architecture and surface potential change of the overlapped GaAsSb/MoS_2 heterojunction. Figure 3b shows the AFM topography image of the overlapped heterojunction region. Also, the extracted AFM height profile in Figure 3e verifies that the thickness of the GaAsSb NW beneath the multilayered MoS_2 flake is ~146 nm, which is similar to the value obtained in Figure 2c. The corresponding KPFM surface potential image of the same region is displayed in Figure 3c under dark conditions. The high contrast in surface potential reveals that the work function is evidently lower in the MoS_2 nanoflake than the GaAsSb NW.[54] Upon the two semi-

https://doi.org/10.1021/acsnano.2c03673
ACS Nano XXXX, XXX, XXX−XXX

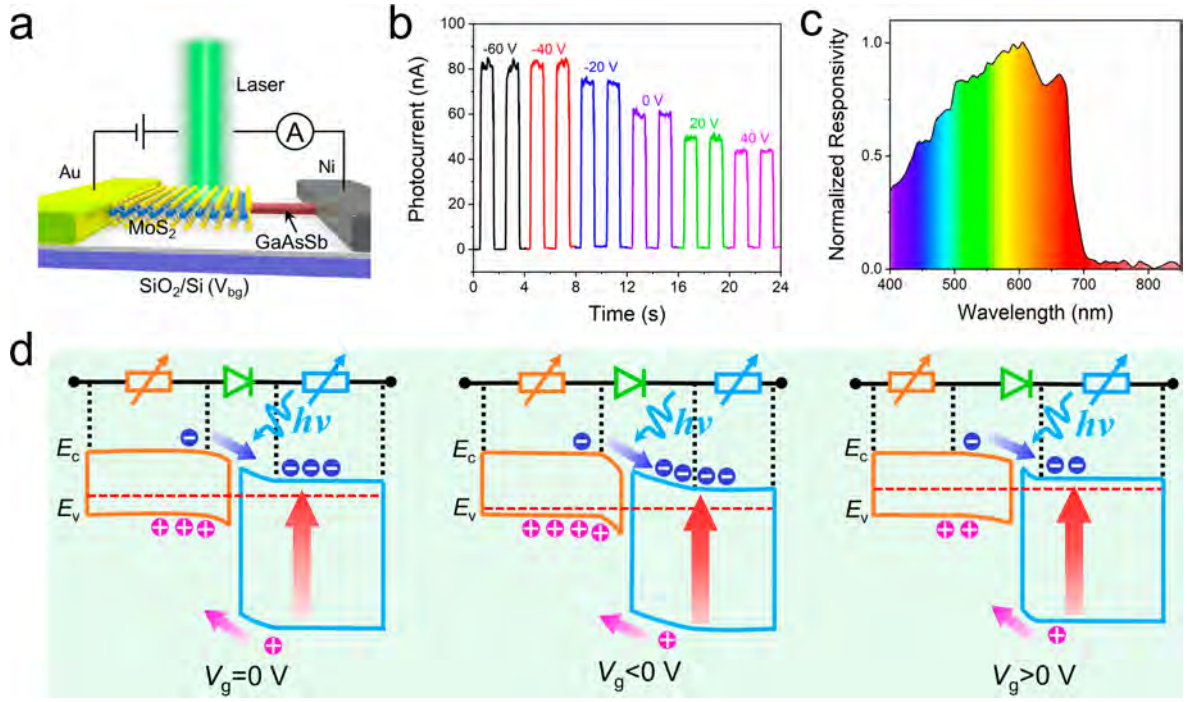

Figure 4. Photoresponse and band diagram variations with gate bias. (a) Device schematic of the GaAsSb/MoS_2 p−n heterojunction photodetector. (b) Time-resolved photoresponse of the GaAsSb/MoS_2 heterostructure device as a function of V_{gs} (532 nm light with the power density of 3.62 mW mm^{-2}). (c) Normalized spectral response of the GaAsSb/MoS_2 heterojunction photodiode under the illumination of 400−850 nm light. (d) Schematic of the energy band diagrams of the GaAsSb/MoS_2 heterojunction at V_{gs} = 0 V, < 0 V, and > 0 V, respectively.

conductors coming into contact, therefore, the electrons would diffuse from MoS_2 to GaAsSb to form a built-in potential drop with a depletion layer across the heterointerface. Figure 3f plots the line profile of the surface potential across the MoS_2−overlapped junction−MoS_2 surface from Figure 3c. Interestingly, after fitting the left and right half of the curve individually by a sigmoidal function, a nearly symmetric distribution of the surface potential is well presented in terms of the Fermi level distinction (~60 mV).[55] The homogeneity in contact potential distribution proves the pronounced interfacial coupling effect once again. Moreover, after contacting with the GaAsSb NW, the magnitude of the downward shift of the Fermi level in MoS_2 is close to the potential difference proposed in the band alignment in Figure 2j. In practice, the built-in voltage (V_{bi}) should be larger than the Fermi level distinction in MoS_2 (namely, V_{bi} > 60 mV) when the equilibrium condition is achieved at the heterointerface.

Since the overlapped junction is not in the same plane as the MoS_2 flake, it is difficult to obtain the depletion width in MoS_2 from the KPFM scanning. In this case, a further step was taken to provide more in-depth insight into the operation of the GaAsSb/MoS_2 heterojunction diode by estimating the depletion width (W_p and W_n) from the following formulas:

$$W_p = \sqrt{\frac{2N_d\varepsilon_a\varepsilon_d V_{bi}}{qN_a(\varepsilon_a N_a + \varepsilon_d N_d)}} \quad (2)$$

$$W_n = \sqrt{\frac{2N_a\varepsilon_a\varepsilon_d V_{bi}}{qN_d(\varepsilon_a N_a + \varepsilon_d N_d)}} \quad (3)$$

where N_a/N_d represents the acceptor/donor concentration, which could be calculated by the equation $n = \sigma/(q\mu)$ from the FET characteristics in Figures S3 and S4 (σ and μ denote the channel conductivity and mobility, respectively; thus N_a = 1.54 × 10^{17} cm^{-3} and N_d = 7.12 × 10^{16} cm^{-3} with the detailed calculation process illustrated in Supplementary Note 1). ε_a and ε_d are the dielectric constants of GaAsSb and MoS_2 ($\varepsilon_d \approx 4$).[56] According to the permittivity of GaAs (ε_{GaAs} = 12.9) and GaSb (ε_{GaSb} = 15.7),[57,58] the ε_a value is calculated to be about 15.4 for the GaAsSb with a 12.0% As composition. Therefore, the W_p and W_n values are estimated to be larger than 8.4 and 18.2 nm for a V_{bi} of over 60 mV. This indicates that MoS_2 contributes more to the photocurrent generation when the hybrid device works as a photodiode without gate bias. It is also clear from eqs 2 and 3 that the W_p and W_n values highly correlate with the built-in voltage and carrier concentration, both of which are determined by the gate-tunable Fermi levels in GaAsSb and MoS_2. As a consequence, the photoresponse of the mixed-dimensional heterojunction diode can be readily modulated with the gate coupling effect.

Through external back-gate modulation, the impact of gate bias on the photodetection performance of the GaAsSb/MoS_2 heterojunction diode was then explored. Figure 4a presents a schematic illustration of the GaAsSb/MoS_2 heterostructure phototransistor on the 270 nm SiO_2/Si substrate, where the laser response was measured under a reverse bias (V_{ds} = −2 V) at different V_{gs} levels. The time-resolved photocurrent as a function of applied back-gate voltage under 532 nm light illumination is shown in Figure 4b. In all curves, the current rises rapidly when a laser is introduced and decays promptly when the laser shutter is closed. Besides, it is interesting that the photocurrent increases starkly as V_{gs} varies from 40 to −40 V and finally reaches a saturation at −60 V as shown in Figure S7b. This similar phenomenon can also be observed from the color plot of the photocurrent at all V_{gs} levels (Figure S7c). The change in photocurrent can be attributed to the band

https://doi.org/10.1021/acsnano.2c03673
ACS Nano XXXX, XXX, XXX−XXX

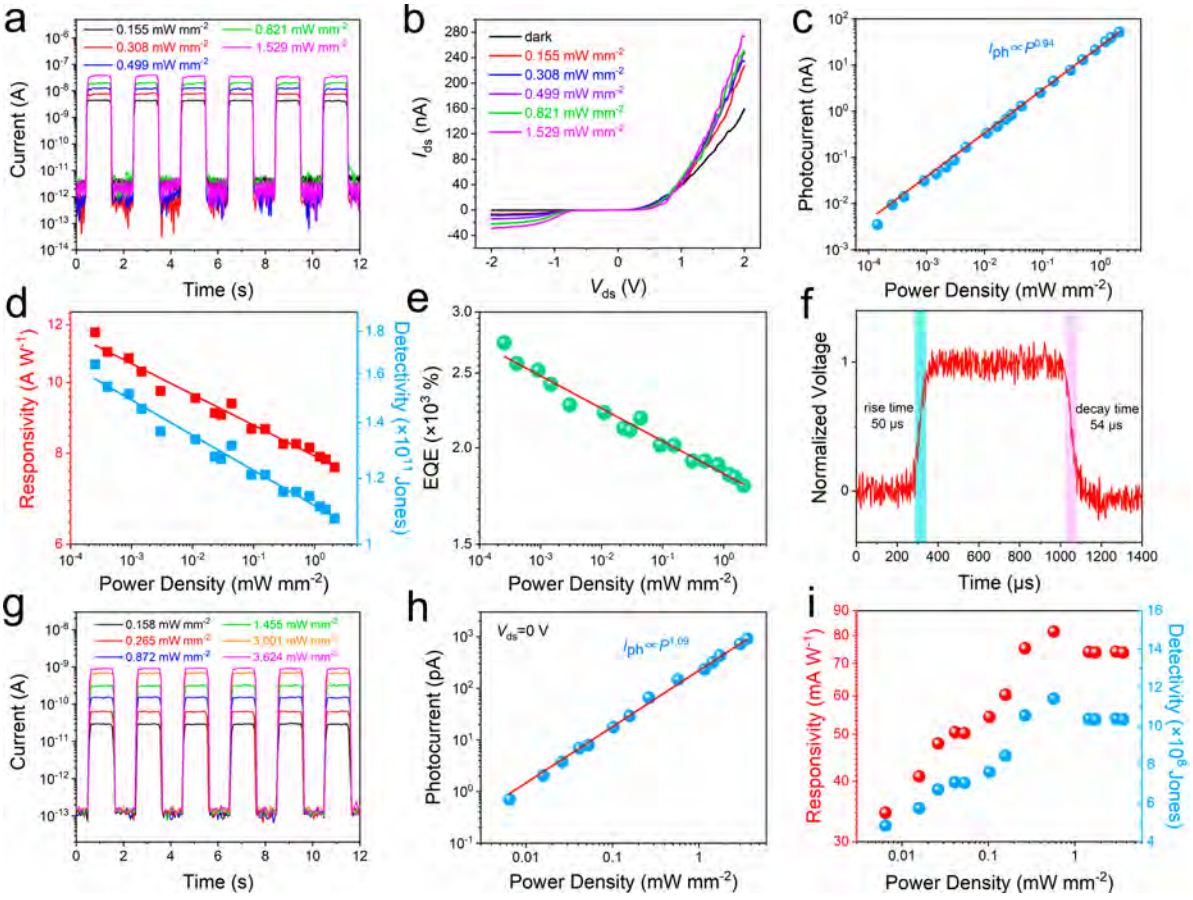

Figure 5. Optoelectronic properties of the GaAsSb/MoS_2 heterostructure device under the illumination of 532 nm light (V_{ds} = −2 V and V_{gs} = −40 V): (a) Reproducible on/off switching under the chopped light illumination (0.155, 0.308, 0.499, 0.821, and 1.529 mW mm^{-2}) using a logarithmic *y*-axis. (b) Current−voltage curves under various illumination intensities. (c) Photocurrent, (d) responsivity, detectivity, and (e) EQE as a function of illumination intensity. (f) High-resolution photoresponse of the heterojunction device to indicate the rise and decay time constants. Photovoltaic response of the GaAsSb/MoS_2 heterostructure device under the illumination of 532 nm light: (g) Reproducible on/off switching under the chopped light illumination using a logarithmic *y*-axis. (h) Photocurrent and (i) responsivity and detectivity as a function of illumination intensity.

structure adjustment in each semiconductor, which occurs in response to the external applied V_{gs}. An obvious decrease in the photocurrent indicates a weakened band bending or built-in voltage at the heterointerface under higher V_{gs}. To further understand the working mechanism of this photodiode, the spectral response characterization was performed from 400 to 850 nm. The wavelength dependence of photoresponsivity in Figure 4c shows two prominent peaks within the range from 600 to 700 nm, which are caused by the spin−orbital splitting of the valence band in MoS_2.[59] Also, the cutoff responsivity of the GaAsSb/MoS_2 photodiode is around 690 nm (~1.8 eV), which is consistent with the PL results of MoS_2 presented in Figure 3a. Hence, the spectral response reveals that the photoresponse of the hybrid photodiode mainly stems from the MoS_2 nanoflake, well corroborating the aforesaid depletion width calculation results showing that MoS_2 dominates the photocurrent generation in the heterojunction. On the other hand, the optical absorption of MoS_2 in the overlapped junction is estimated to be more than three times larger than that of the GaAsSb NW segment in the visible band (Supplementary Note 2), further demonstrating the major role of MoS_2 in the measured photoresponse.

In light of the above discoveries, the band structure evolution with gate bias is then proposed to account for the gate tunability of the photocurrent in Figure 4d. As known from Figure 2j, a type II heterostructure is formed between GaAsSb and MoS_2. At V_{gs} = 0 V, the higher Fermi level in MoS_2 would facilitate electron transfer to GaAsSb until a thermal equilibrium state is reached in the system, giving rise to the band bending downward in GaAsSb and upward in MoS_2. Due to the larger depletion width and stronger optical absorption, the photocarriers would be mostly produced in MoS_2 under exposure to incident light, which is followed by a fast separation process at the interface and thus the generation of photocurrent. When the back-gate bias is applied, the doping level in each semiconductor can be modulated, which dictates the depletion width and slope of band bending at the heterointerface. Specifically, as the gate voltage becomes negative (V_{gs} < 0 V), the n-type MoS_2 flake changes from n doped to a nearly insulating state at V_{gs} = −60 V, whereas the p-type GaAsSb experiences an opposite change as the carriers are positively charged. In this case, the depletion region in the p−n heterojunction extends farther into the side with low doping/majority carrier concentration; then the junction almost entirely lies in MoS_2 as it is depleted at negative V_{gs}, leading to an increased photocurrent contribution from the MoS_2 portion.[16] Accordingly, the impact of relatively reduced photocurrent in GaAsSb is insignificant to the total photo-

https://doi.org/10.1021/acsnano.2c03673
ACS Nano XXXX, XXX, XXX−XXX

Table 1. Performance Comparison of the GaAsSb/MoS_2 Heterostructure Phototransistor with Other Mixed-Dimensional and 2D Material-Based Photodiodes

photodetector	wavelength (nm)	I_{on}/I_{off}	responsivity (A W^{-1})	detectivity (Jones)	rise/decay time	ref
1D Sb_2Se_3/2D WS_2	520	334	1.51	1.16×10^{10}	<8 ms	66
1D ZnO/2D WSe_2	520	$<10^2$	0.67			44
SWCNT/MoS_2	650		0.1		15 μs	16
2D WSe_2/SnS_2	520		0.1	4.71×10^{10}	500/600 μs	63
2D GaSe/3D VO_2	405	433	0.358	2.14×10^{11}		65
2D PtS_2/WSe_2	635	10^5	1.7	3.8×10^{10}	8/9 μs	67
2D GaSe/MoS_2	532	$>10^2$	0.05	10^{10}	50 ms	68
2D AsP/InSe	520	1×10^7	1	1×10^{12}	217/89 μs	69
1D GaAsSb/2D MoS_2	532	4×10^4	11.7	1.64×10^{11}	50/54 μs	this work

response because of the weak optical absorption. Moreover, the higher negative V_{gs} corresponds to pushing down the Fermi level in the band diagram. This would result in the change of band alignment by augmenting the band bending, helping to separate the photoinduced electron−hole pairs more efficiently.[16,41] As a consequence, with decreasing gate voltage, the increased p-doping of the GaAsSb NWs and associated decreased n-doping of MoS_2 lead to a higher photocurrent. On the contrary, when V_{gs} is scanned from 0 to 40 V, the shifted conducting state of the heterojunction exerts a passive influence on the depletion region in MoS_2 and band bending. This way, an adverse change would be expected in the photogeneration and charge carrier transfer across the heterojunction. Based on the electrical analysis, it is verified that the band alignment of the mixed-dimensional GaAsSb/MoS_2 heterostructure can be effectively tuned by the capacitively coupled gate bias, therefore affecting the photodetection performance of the p−n diode.

At a back-gate voltage of −40 V, the GaAsSb/MoS_2 anti-ambipolar phototransistor exhibits a strong photoresponse, which can be exploited as a photodetector. Meanwhile, based on the anti-ambipolar transfer curve in Figure 2e, it is clear that the peak I_{on} (~220 nA) lies at V_{gs} of −40 V. As key parameters to quantify the diode performance, the best rectification ratio and ideality factor are also achieved at the same value. Therefore, such a gate bias would be the optimal condition for balanced electron−hole carrier concentration. The photodetection performance of the GaAsSb/MoS_2 heterojunction diode was then characterized under a constant source−drain bias (V_{ds} = −2 V) and a gate bias (V_{gs} = −40 V). When irradiated at varying power intensities, it is revealed that the as-fabricated photodiode yields good repeatability and stability by periodically modulating the 532 nm laser at a chopped frequency of 0.5 Hz (Figure 5a). Since the device works in the off-state at V_{ds} < 0, the photogenerated carriers become dominated to bring about a significant current increase upon illumination. It is worth noting that a high I_{on}/I_{off} ratio of ~4×10^4 is attained under an intensity of 1.529 mW mm^{-2}, unveiling its high ability to detect optical signals. The typical output current−voltage characteristics of the GaAsSb/MoS_2 heterostructure photodetector with and without illumination of 532 nm are demonstrated in Figure 5b. With the increasing light power density, the illuminated output current increases accordingly under a V_{ds} of −2 V, suggesting the effective photoresponse of the hybrid phototransistor. To further evaluate the photoresponse characteristics, the light intensity dependence of the measured photocurrent I_{ph} (defined as $I_{ph} = I_{light} - I_{dark}$) is compiled in Figure 5c, in which the relationship can be fitted by the power law equation:

$$I_{ph} = AP^{\alpha} \tag{4}$$

where A and α are the scaling constant and the fitting exponent, respectively, and P is the light intensity. Through fitting, the photocurrent displays a power dependence of 0.94. This nearly linear relationship between photocurrent and light intensity indicates a superior photon-to-electron conversion efficiency. Theoretically, owing to the formation of a type II band alignment along with the high-quality heterointerface, the good linearity primarily stems from the photovoltaic effect that dominates the photocurrent response in the GaAsSb/MoS_2 heterojunction. Hence, the photoexcited carriers can be separated efficiently within the depletion region, instead of accumulating or being trapped at the interface to form charge-transfer dipoles, hindering the further charge transport of photogenerated electrons and holes.

On the other hand, photoresponsivity (R), detectivity (D^*), and external quantum efficiency (EQE) are other figures of merit to evaluate the device performance, which can be defined as

$$R = \frac{I_{ph}}{PS} \tag{5}$$

$$D^* = R\sqrt{\frac{S}{2eI_{dark}}} \tag{6}$$

$$\mathrm{EQE} = R\frac{hc}{e\lambda} \tag{7}$$

where S is the effective irradiated area, e is the electronic charge, h is Planck's constant, c is the velocity of light, and λ is the incident wavelength.[60] Based on the above equations, the light intensity dependent R, D^*, and EQE are calculated and depicted in Figure 5d and e. Notably, all these three values give a decreasing tendency with the increasing light intensity because the carrier recombination would be intensified at a relatively higher power density.[61,62] Under a low light intensity of 0.26 μW mm^{-2}, the R value is found to be as high as 11.7 A W^{-1}, and the corresponding D^* and EQE values are up to 1.64×10^{11} Jones and 2.74×10^3%, respectively. The R value is as least 1 order of magnitude higher than those of visible-light photodetectors based on the 1D ZnO/2D WSe_2 vdW heterojunction (0.67 A W^{-1}),[44] WSe_2/SnS_2 vertical heterostructure (108.7 mA W^{1-}),[63] and SWCNT/MoS_2 p−n diode (0.1 A W^{-1}).[16] As an important device parameter, the response speed can reflect the ability of a photodetector to follow the rapidly varied optical signals. The temporal photoresponse to an ultrafast pulse laser of 532 nm was investigated and monitored by an oscilloscope, as shown in Figure 5f and Figure

https://doi.org/10.1021/acsnano.2c03673
ACS Nano XXXX, XXX, XXX−XXX

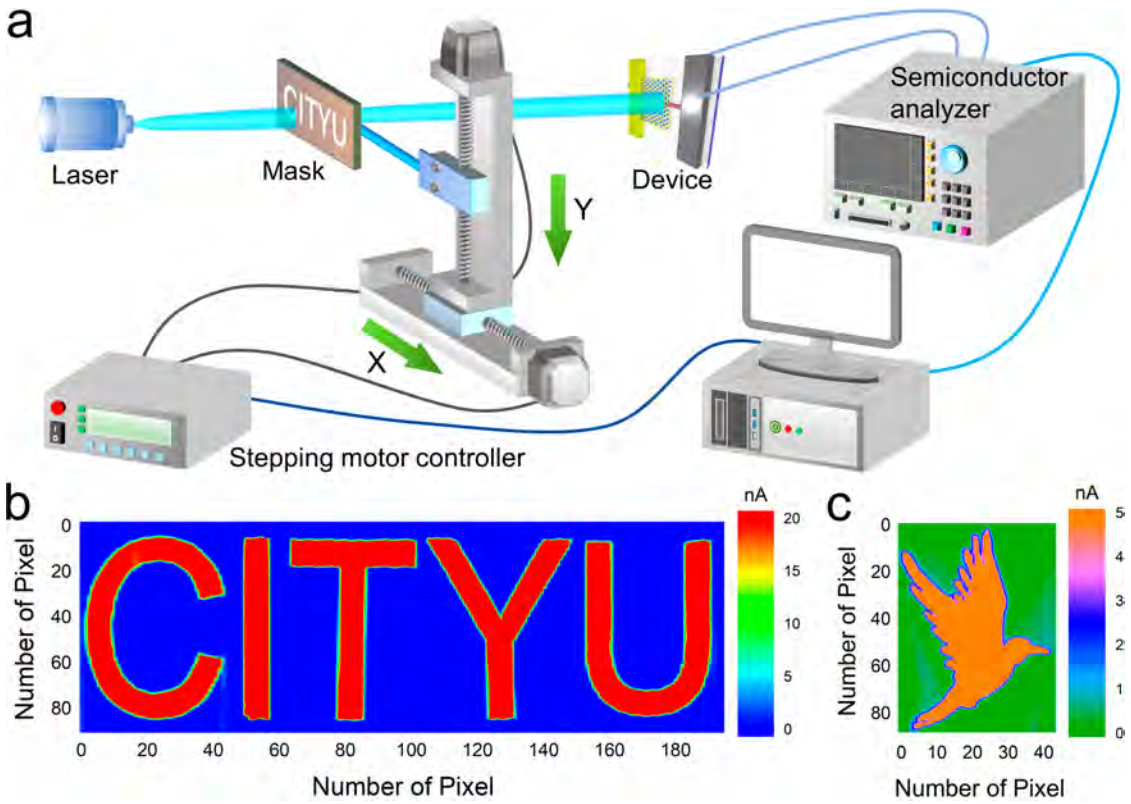

Figure 6. Image sensing application of the GaAsSb/MoS_2 heterostructure photodiode: (a) Schematic diagram of the image scanning system of the GaAsSb/MoS_2 heterojunction imager. The corresponding current mapping of the images of (b) "CITYU" and (c) a flying bird under 532 nm illumination.

S8. Then, the rise and decay times, defined as the time interval between 10% and 90% of the peak value of the photocurrent, accordingly, can be extracted from the high-resolution photoresponse measurement given in Figure 5f. The rise and decay times are determined to be 50 and 54 μs, respectively, indicating the very fast response of the device. Next, the frequency bandwidth (f_{3dB}) of the heterostructure can be estimated to be ~10^4 Hz from the response time ($\tau = 0.55/f_{3dB}$).[19] In contrast, both the unipolar GaAsSb and MoS_2 phototransistors show much longer response times (>2 s) due to the severe persistent photoconductivity (PPC), as shown in Figures S9–S11, which have also been reported in other previous works.[64,65] Since the configuration of the GaAsSb/MoS_2 heterojunction is capable of suppressing the PPC phenomena, the response speed can be simply enhanced by the formation of a p–n junction at a vdW heterointerface here. Table 1 summarizes the major device parameters of the GaAsSb/MoS_2 heterostructure photodetector obtained under 532 nm illumination, which are very competitive as compared with other reported 2D materials-based photodiodes.

Operated at a zero source–drain bias, the heterostructure device also shows an obvious photovoltaic response under 532 nm irradiation. The presence of a built-in electric field evidenced in the KPFM test delivers a significant contribution to the suppression of dark current noise and the separation of photocarriers. The dark current of the device is as low as ~100 fA from the reproducible on/off switching behaviors as shown in Figure 5g, which yields a high on–off current ratio of ~1×10^4 at a light intensity of 3.624 mW mm^{-2}. Linear dynamic range (LDR), another essential index for photodetectors, is normally brought in to assess the imaging performance of photodetectors, which is given by

$$\mathrm{LDR} = 20 \log(I_{light}/I_{dark}) \tag{8}$$

Generally, for the imaging application of photodetectors, the ratio of full-well capacity of complementary metal-oxide-semiconductor image sensors to dark electrons is required to be over 60 dB. Although the heterostructure device is manipulated at V_{ds} = 0 V, the LDR is still calculated to be 80 dB according to the photoswitching curve, which is considerably higher than the commercialized InGaAs photodiodes (66 dB).[70,71] The photovoltaic effect revealed from the I_{ds}–V_{ds} curves indicates that the open-circuit voltage (V_{oc}) increases gradually with light intensity and can reach up to ~0.2 V at 3.624 mW mm^{-2} (Figure S12a). This is because the V_{oc} value is positively correlated to the charge generation rate that is proportional to the light intensity.[72] Moreover, a modified Shockley diode equation is exploited to fit the I_{ds}–V_{ds} characteristics in the photovoltaic region (Figure S12b):

$$I(V) = I_{ph}\left\{\exp\left[\frac{q(V - V_{oc})}{k_B T(1 + \delta)}\right] - 1\right\} \tag{9}$$

Here, δ is a dimensionless quantity that depends on charge recombination and extraction. A δ value of ~3, for 0.158 and 3.001 mW mm^{-2} light illumination, indicates good carrier extraction at the contacts.[73] The photocurrent *versus* incident power follows a power law with $\alpha > 1$, as shown in Figure 5h. This unusual superlinear behavior can be explained by the presence of intragap recombination centers with different energies and capture cross sections in MoS_2 (Supplementary

https://doi.org/10.1021/acsnano.2c03673
ACS Nano XXXX, XXX, XXX–XXX

Note 3).[74] Using eqs 5−7, the extracted R, D^*, and EQE values are demonstrated in Figure 5i and Figure S12c, all of which show an overall upward trend with the increasing light intensity due to the drop of recombination rate at high power intensity.[75] Given the adequate built-in voltage at the heterointerface would prolong the carrier lifetime and shorten the transient time of photocarriers, the heterostructure photovoltaic device yields a fast response speed. The photoresponse time reported here is limited by the current resolution of the preamplifier used in this experiment, and thus rise/decay times of 98/79 ms represent an upper bound (Figure S12d). Apart from the 532 nm photodetection, the comparable photoresponse properties of the GaAsSb/MoS_2 heterojunction device in both the reverse-biased and photovoltaic regions are also achieved under 635 nm illumination (Figures S13, S14). Such respectable results obtained above can be attributed to the superior crystal quality and high mobility of constituent semiconductors and the unique physical properties of the heterostructure, such as gate-tunability, fast charge separation, strong interfacial coupling effect, *etc.*

In consideration of the high photosensitivity in the visible light region, the GaAsSb/MoS_2 anti-ambipolar phototransistor holds good potential for image sensing applications. The imaging capability of this device was explored by the setup as schematically illustrated in Figure 6a. A 532 nm laser was used for the light source and placed in front of the image mask; then the light beam could pass through the hollowed-out pattern and shed on the heterostructure photodetector. With the movement of the image mask controlled by the $X-Y$ planar moving stage, the spatially resolved photoresponse of the device could then be recorded by the computer connecting with a semiconductor analyzer in real time, coming into being images of both "CITYU" and a flying bird with high resolution (Figure 6b,c). As the 532 nm light spot scans the image mask "CITYU" along the Y direction with represented X-direction pixel sequences, the resulting time-resolved current curves of the GaAsSb/MoS_2 heterojunction photodiode are displayed in Figure S15, confirming the high stability and photosensitivity of the imaging system. These impressive results evidently herald the promising imaging applications of GaAsSb/MoS_2 heterojunction phototransistors.

CONCLUSIONS

In summary, we developed an anti-ambipolar phototransistor through the vdW bonding of 1D p-type GaAsSb NW and 2D n-type MoS_2 nanoflake. When operated as a three-terminal field-effect transistor, the hybrid device shows the obvious anti-ambipolar behavior that results from the change in series resistance, suggesting its potency in advanced logic applications. The gate-tunability was well studied by analyzing the electrical and optoelectronic properties of devices with gate modulation. The photodiode exhibits a quick and sensitive response to visible incident light because of the band engineering by varying the gate bias, while the depletion region at the heterointerface is found to play a crucial role in controlling the photoresponse of the p−n device. In particular, the band bending and extension of the depletion region across the vdW interface can be tuned by gating, influencing the separation efficiency of photogenerated carriers. Ultimately, a high-resolution visible image sensor using the GaAsSb/MoS_2 heterojunction phototransistor as single pixel has been demonstrated to identify its good imaging capability. All these impressive features signify the versatility of mixed-dimensional vdW heterostructures, bringing prospects for next-generation electronics and optoelectronics.

METHODS

Nanowire Synthesis and Measurement. The GaAsSb NWs were synthesized through a solid-source CVD method in a dual-zone horizontal tube furnace. First, a 0.5 nm Au catalyst film was predeposited on SiO_2/Si substrates (50 nm thick thermally grown oxide) by thermal evaporation. Then, the solid source, well-mixed GaSb/GaAs with a mass ratio of 20:1 in wt %, was placed in the center of the quartz tube of the upstream zone, while the SiO_2/Si substrates with predeposited Au film were positioned in the downstream zone (~12 cm away from the solid source). After pumping down the system to 2×10^{-3} Torr, the high-purity H_2 as a carrier gas with a flow rate of 100 sccm was brought into the CVD system, and the pressure of the chamber was maintained at 1.8 Torr. During the NW growth, the source and substrate were heated to 730 and 600 °C in 8 min, respectively, which were subsequently kept for a duration of 10 min. After growth, the system was cooled to the ambient temperature in a H_2 atmosphere. The surface morphologies of the grown GaAsSb NWs were characterized by SEM (XL30, FEI/Philips) and TEM (CM-20, Philips). The crystal structures were determined by studying the XRD patterns and imaging with high-resolution TEM (Tecnai G^2 F30, FEI). The elemental compositions were tested by the EDS attached to the Philips CM20. The band structure of the synthesized GaAsSb NWs was determined by UV−vis−NIR spectroscopy (Lambda 750, PerkinElmer) and UPS (ESCALAB 250XI, ThermoFisher).

Device Fabrication and Characterization. The prepared GaAsSb NWs were transferred on the 270 nm thick SiO_2/Si substrates by a dry transfer technique, followed by standard photolithography and e-beam evaporation to define and deposit the 60 nm thick Ni contact (Figure S2). The MoS_2 nanoflake was mechanically exfoliated by polydimethylsiloxane (PDMS) and then transferred accurately onto the GaAsSb NW using a micromanipulation transfer system, forming the GaAsSb/MoS_2 vdW heterojunction. After that, a Au electrode (60 nm) on top of the MoS_2 was subsequently patterned by electron beam lithography and thermal evaporation. The height profiles and surface potential difference of the GaAsSb NW and MoS_2 nanoflake were evaluated by AFM (Dimension Icon, Bruker), and the Raman and PL spectra were both measured by a confocal microscope spectrometer (Alpha 300R, WITec). The electronic and optoelectronic performance were carried out with an Agilent 4155C semiconductor analyzer and a standard electrical probe station under illumination of laser sources (532 and 635 nm), whose power was calibrated and measured by a power meter (PM400, Thorlabs). High-resolution time response curves of the heterojunction diode were recorded by a digital oscilloscope (TBS 1102B-EDU, Tektronix) combined with a low-noise current preamplifier (SR570, Stanford Research Systems).

ASSOCIATED CONTENT

Supporting Information

The Supporting Information is available free of charge at https://pubs.acs.org/doi/10.1021/acsnano.2c03673.

UV−vis−NIR DRS absorption spectrum and energy band structure; schematics of device fabrication procedures; FET properties of GaAsSb NWs and MoS_2 nanoflakes; $I-V$ plots of the heterojunction device; photocurrent as a function of gate bias; high-resolution transient photoresponse characterization; optoelectronic properties of GaAsSb NWs and MoS_2 nanoflake phototransistors; optoelectronic properties and photovoltaic response of the heterostructure device; time-resolved current curves of the GaAsSb/MoS_2 image sensor; optical absorption calculation method (PDF)

https://doi.org/10.1021/acsnano.2c03673
ACS Nano XXXX, XXX, XXX−XXX

AUTHOR INFORMATION

Corresponding Author

Johnny C. Ho − *Department of Materials Science and Engineering, State Key Laboratory of Terahertz and Millimeter Waves, and Hong Kong Institute for Advanced Study, City University of Hong Kong, Kowloon 999077 Hong Kong SAR, China; Institute for Materials Chemistry and Engineering, Kyushu University, Fukuoka 816-8580, Japan*; Email: johnnyho@cityu.edu.hk

Authors

Wei Wang − *Department of Materials Science and Engineering, City University of Hong Kong, Kowloon 999077 Hong Kong SAR, China*

Weijun Wang − *Department of Materials Science and Engineering, City University of Hong Kong, Kowloon 999077 Hong Kong SAR, China*

You Meng − *Department of Materials Science and Engineering, City University of Hong Kong, Kowloon 999077 Hong Kong SAR, China*

Quan Quan − *Department of Materials Science and Engineering, City University of Hong Kong, Kowloon 999077 Hong Kong SAR, China*

Zhengxun Lai − *Department of Materials Science and Engineering, City University of Hong Kong, Kowloon 999077 Hong Kong SAR, China*

Dengji Li − *Department of Materials Science and Engineering, City University of Hong Kong, Kowloon 999077 Hong Kong SAR, China*

Pengshan Xie − *Department of Materials Science and Engineering, City University of Hong Kong, Kowloon 999077 Hong Kong SAR, China*

SenPo Yip − *Institute for Materials Chemistry and Engineering, Kyushu University, Fukuoka 816-8580, Japan*

Xiaolin Kang − *Department of Materials Science and Engineering, City University of Hong Kong, Kowloon 999077 Hong Kong SAR, China*

Xiuming Bu − *Department of Materials Science and Engineering, City University of Hong Kong, Kowloon 999077 Hong Kong SAR, China*; orcid.org/0000-0002-2372-2271

Dong Chen − *Department of Materials Science and Engineering, City University of Hong Kong, Kowloon 999077 Hong Kong SAR, China*

Chuntai Liu − *Key Laboratory of Advanced Materials Processing & Mold (Zhengzhou University), Ministry of Education, Zhengzhou 450002, China*; orcid.org/0000-0001-9751-6270

Complete contact information is available at: https://pubs.acs.org/10.1021/acsnano.2c03673

Author Contributions

The work was accomplished through contributions of all authors. All authors have given approval to the final version of the manuscript.

Notes

The authors declare no competing financial interest.

ACKNOWLEDGMENTS

This research was financially supported by a fellowship award from the Research Grants Council of the Hong Kong Special Administrative Region, China (CityU RFS2021-1S04), and the Shenzhen Municipality Science and Technology Innovation Commission (grant no. SGDX20201103093004O2; "Modulation and Detection of Terahertz Waves based on Semi-Metallic Two-Dimensional Materials", CityU).

REFERENCES

(1) Geim, A. K.; Grigorieva, I. V. Van der Waals Heterostructures. *Nature* **2013**, *499*, 419−425.

(2) Jariwala, D.; Sangwan, V. K.; Lauhon, L. J.; Marks, T. J.; Hersam, M. C. Emerging Device Applications for Semiconducting Two-Dimensional Transition Metal Dichalcogenides. *ACS Nano* **2014**, *8*, 1102−1120.

(3) Furchi, M. M.; Pospischil, A.; Libisch, F.; Burgdorfer, J.; Mueller, T. Photovoltaic Effect in an Electrically Tunable van der Waals Heterojunction. *Nano Lett.* **2014**, *14*, 4785−4791.

(4) Liu, Y.; Wu, H.; Cheng, H. C.; Yang, S.; Zhu, E. B.; He, Q. Y.; Ding, M. N.; Li, D. H.; Guo, J.; Weiss, N. O.; Huang, Y.; Duan, X. F. Toward Barrier Free Contact to Molybdenum Disulfide Using Graphene Electrodes. *Nano Lett.* **2015**, *15*, 3030−3034.

(5) Cheng, R.; Li, D. H.; Zhou, H. L.; Wang, C.; Yin, A. X.; Jiang, S.; Liu, Y.; Chen, Y.; Huang, Y.; Duan, X. F. Electroluminescence and Photocurrent Generation from Atomically Sharp WSe_2/MoS_2 Heterojunction p-n Diodes. *Nano Lett.* **2014**, *14*, 5590−5597.

(6) Li, D. H.; Cheng, R.; Zhou, H. L.; Wang, C.; Yin, A. X.; Chen, Y.; Weiss, N. O.; Huang, Y.; Duan, X. F. Electric-Field-Induced Strong Enhancement of Electroluminescence in Multilayer Molybdenum Disulfide. *Nat. Commun.* **2015**, *6*, 7509.

(7) Palacios-Berraquero, C.; Barbone, M.; Kara, D. M.; Chen, X. L.; Goykhman, I.; Yoon, D.; Ott, A. K.; Beitner, J.; Watanabe, K.; Taniguchi, T.; Ferrari, A. C.; Atature, M. Atomically Thin Quantum Light-Emitting Diodes. *Nat. Commun.* **2016**, *7*, 12978.

(8) Li, D.; Chen, M. Y.; Sun, Z. Z.; Yu, P.; Liu, Z.; Ajayan, P. M.; Zhang, Z. X. Two-Dimensional Non-Volatile Programmable p-n Junctions. *Nat. Nanotechnol.* **2017**, *12*, 901−906.

(9) Wu, L. M.; Wang, A. W.; Shi, J. A.; Yan, J. H.; Zhou, Z.; Bian, C.; Ma, J. J.; Ma, R. S.; Liu, H. T.; Chen, J. C.; Huang, Y.; Zhou, W.; Bao, L. H.; Ouyang, M.; Pennycook, S. J.; Pantelides, S. T.; Gao, H. J. Atomically Sharp Interface Enabled Ultrahigh-Speed Non-Volatile Memory Devices. *Nat. Nanotechnol.* **2021**, *16*, 882−887.

(10) Yang, H.; Heo, J.; Park, S.; Song, H. J.; Seo, D. H.; Byun, K. E.; Kim, P.; Yoo, I.; Chung, H. J.; Kim, K. Graphene Barristor, a Triode Device with a Gate-Controlled Schottky Barrier. *Science* **2012**, *336*, 1140−1143.

(11) Lee, H. S.; Baik, S. S.; Lee, K.; Min, S. W.; Jeon, P. J.; Kim, J. S.; Choi, K.; Choi, H. J.; Kim, J. H.; Im, S. Metal Semiconductor Field-Effect Transistor with MoS_2/Conducting NiO_x van der Waals Schottky Interface for Intrinsic High Mobility and Photoswitching Speed. *ACS Nano* **2015**, *9*, 8312−8320.

(12) Shokouh, S. H. H.; Pezeshki, A.; Raza, S. R. A.; Lee, H. S.; Min, S. W.; Jeon, P. J.; Shin, J. M.; Im, S. High-Gain Subnanowatt Power Consumption Hybrid Complementary Logic Inverter with WSe_2 Nanosheet and ZnO Nanowire Transistors on Glass. *Adv. Mater.* **2015**, *27*, 150−156.

(13) Shim, J.; Jo, S. H.; Kim, M.; Song, Y. J.; Kim, J.; Park, J. H. Light-Triggered Ternary Device and Inverter Based on Heterojunction of van der Waals Materials. *ACS Nano* **2017**, *11*, 6319−6327.

(14) Britnell, L.; Gorbachev, R. V.; Jalil, R.; Belle, B. D.; Schedin, F.; Mishchenko, A.; Georgiou, T.; Katsnelson, M. I.; Eaves, L.; Morozov, S. V.; Peres, N. M. R.; Leist, J.; Geim, A. K.; Novoselov, K. S.; Ponomarenko, L. A. Field-Effect Tunneling Transistor Based on Vertical Graphene Heterostructures. *Science* **2012**, *335*, 947−950.

(15) Qian, X. F.; Liu, J. W.; Fu, L.; Li, J. Quantum Spin Hall Effect in Two-Dimensional Transition Metal Dichalcogenides. *Science* **2014**, *346*, 1344−1347.

(16) Jariwala, D.; Sangwan, V. K.; Wu, C. C.; Prabhumirashi, P. L.; Geier, M. L.; Marks, T. J.; Lauhon, L. J.; Hersam, M. C. Gate-Tunable Carbon Nanotube-MoS_2 Heterojunction p-n Diode. *P. Natl. Acad. Sci.* **2013**, *110*, 18076−18080.

https://doi.org/10.1021/acsnano.2c03673
ACS Nano XXXX, XXX, XXX−XXX

(17) Jariwala, D.; Sangwan, V. K.; Seo, J. W. T.; Xu, W. C.; Smith, J.; Kim, C. H.; Lauhon, L. J.; Marks, T. J.; Hersam, M. C. Large-Area, Low-Voltage, Antiambipolar Heterojunctions from Solution-Processed Semiconductors. *Nano Lett.* **2015**, *15*, 416−421.
(18) Jariwala, D.; Howell, S. L.; Chen, K. S.; Kang, J. M.; Sangwan, V. K.; Filippone, S. A.; Turrisi, R.; Marks, T. J.; Lauhon, L. J.; Hersam, M. C. Hybrid, Gate-Tunable, van der Waals p-n Heterojunctions from Pentacene and MoS_2. *Nano Lett.* **2016**, *16*, 497−503.
(19) Huo, N. J.; Yang, J. H.; Huang, L.; Wei, Z. M.; Li, S. S.; Wei, S. H.; Li, J. B. Tunable Polarity Behavior and Self-Driven Photoswitching in p-WSe_2/n-WS_2 Heterojunctions. *Small* **2015**, *11*, 5430−5438.
(20) Paul, A. K.; Kuiri, M.; Saha, D.; Chakraborty, B.; Mahapatra, S.; Sood, A. K.; Das, A. Photo-Tunable Transfer Characteristics in $MoTe_2$-MoS_2 Vertical Heterostructure. *Npj. 2d Mater. Appl.* **2017**, *1*, 17.
(21) Inbaraj, C. R. P.; Mathew, R. J.; Ulaganathan, R. K.; Sankar, R.; Kataria, M.; Lin, H. Y.; Chen, Y. T.; Hofmann, M.; Lee, C. H.; Chen, Y. F. A Bi-Anti-Ambipolar Field Effect Transistor. *ACS Nano* **2021**, *15*, 8686−8693.
(22) Tran, T. U.; Nguyen, D. A.; Duong, N. T.; Park, D. Y.; Nguyen, D. H.; Nguyen, P. H.; Park, C.; Lee, J.; Ahn, B. W.; Im, H. Gate Tunable Photoresponse of a Two-Dimensional p-n Junction for High Performance Broadband Photodetector. *Applied Materials Today* **2022**, *26*, 101285.
(23) Sangwan, V. K.; Hersam, M. C. Electronic Transport in Two-Dimensional Materials. *Annu. Rev. Phys. Chem.* **2018**, *69*, 299−325.
(24) Wang, K. C.; Valencia, D.; Charles, J.; Henning, A.; Beck, M. E.; Sangwan, V. K.; Lauhon, L. J.; Hersam, M. C.; Kubis, T. Atomic-Level Charge Transport Mechanism in Gate-Tunable Anti-Ambipolar van der Waals Heterojunctions. *Appl. Phys. Lett.* **2021**, *118*, 083103.
(25) Yao, H.; Wu, E. X.; Liu, J. Frequency Doubler Based on a Single $MoTe_2$/MoS_2 Anti-Ambipolar Heterostructure. *Appl. Phys. Lett.* **2020**, *117*, 123103.
(26) Li, Y. T.; Wang, Y.; Huang, L.; Wang, X. T.; Li, X. Y.; Deng, H. X.; Wei, Z. M.; Li, J. B. Anti-Ambipolar Field-Effect Transistors Based on Few-Layer 2D Transition Metal Dichalcogenides. *ACS Appl. Mater. Inter.* **2016**, *8*, 15574−15581.
(27) Huang, M. Q.; Li, S. M.; Zhang, Z. F.; Xiong, X.; Li, X. F.; Wu, Y. Q. Multifunctional High-Performance van der Waals Heterostructures. *Nat. Nanotechnol.* **2017**, *12*, 1148−1154.
(28) Yi, S. G.; Kim, J. H.; Min, J. K.; Park, M. J.; Chang, Y. W.; Yoo, K. H. Optoelectric Properties of Gate-Tunable MoS_2/WSe_2 Heterojunction. *IEEE T. Nanotechnol.* **2016**, *15*, 499−505.
(29) Wakayama, Y.; Hayakawa, R. Antiambipolar Transistor: A Newcomer for Future Flexible Electronics. *Adv. Funct. Mater.* **2020**, *30*, 1903724.
(30) Ren, F. F.; Ang, K. W.; Ye, J. D.; Yu, M. B.; Lo, G. Q.; Kwong, D. L. Split Bull's Eye Shaped Aluminum Antenna for Plasmon-Enhanced Nanometer Scale Germanium Photodetector. *Nano Lett.* **2011**, *11*, 1289−1293.
(31) Rezaei, M.; Bianconi, S.; Lauhon, L. J.; Mohseni, H. A New Approach to Designing High-Sensitivity Low-Dimensional Photodetectors. *Nano Lett.* **2021**, *21*, 9838−9844.
(32) Kang, Y. M.; Liu, H. D.; Morse, M.; Paniccia, M. J.; Zadka, M.; Litski, S.; Sarid, G.; Pauchard, A.; Kuo, Y. H.; Chen, H. W.; Zaoui, W. S.; Bowers, J. E.; Beling, A.; McIntosh, D. C.; Zheng, X. G.; Campbell, J. C. Monolithic Germanium/Silicon Avalanche Photodiodes with 340 GHz Gain-Bandwidth Product. *Nat. Photonics* **2009**, *3*, 59−63.
(33) Garnett, E.; Yang, P. D. Light Trapping in Silicon Nanowire Solar Cells. *Nano Lett.* **2010**, *10*, 1082−1087.
(34) Li, N. N.; Wen, Y.; Cheng, R. Q.; Yin, L.; Wang, F.; Li, J.; Shifa, T. A.; Feng, L. P.; Wang, Z. X.; He, J. Strongly Coupled van der Waals Heterostructures for High-Performance Infrared Phototransistor. *Appl. Phys. Lett.* **2019**, *114*, 103501.
(35) Han, N.; Hou, J. J.; Wang, F. Y.; Yip, S.; Yen, Y. T.; Yang, Z. X.; Dong, G. F.; Hung, T.; Chueh, Y. L.; Ho, J. C. GaAs Nanowires: From Manipulation of Defect Formation to Controllable Electronic Transport Properties. *ACS Nano* **2013**, *7*, 9138−9146.
(36) Wang, W.; Yip, S. P.; Meng, Y.; Wang, W. J.; Wang, F.; Bu, X. M.; Lai, Z. X.; Kang, X. L.; Xie, P. S.; Quan, Q.; Liu, C. T.; Ho, J. C. Antimony-Rich $GaAs_xSb_{1-x}$ Nanowires Passivated by Organic Sulfides for High-Performance Transistors and Near-Infrared Photodetectors. *Adv. Opt. Mater.* **2021**, *9*, 2101289.
(37) Li, L. X.; Pan, D.; Xue, Y. Z.; Wang, X. L.; Lin, M. L.; Su, D.; Zhang, Q. L.; Yu, X. Z.; So, H.; Wei, D. H.; Sun, B. Q.; Tan, P. H.; Pan, A. L.; Zhao, J. H. Near Full-Composition-Range High-Quality $GaAs_{1-x}Sb_x$ Nanowires Grown by Molecular-Beam Epitaxy. *Nano Lett.* **2017**, *17*, 622−630.
(38) Jastrzebski, L.; Lagowski, J.; Gatos, H. C. Application of Scanning Electron-Microscopy to Determination of Surface Recombination Velocity: GaAs. *Appl. Phys. Lett.* **1975**, *27*, 537−539.
(39) Li, D. P.; Lan, C. Y.; Manikandan, A.; Yip, S.; Zhou, Z. Y.; Liang, X. G.; Shu, L.; Chueh, Y. L.; Han, N.; Ho, J. C. Ultra-Fast Photodetectors Based on High-Mobility Indium Gallium Antimonide Nanowires. *Nat. Commun.* **2019**, *10*, 1664.
(40) Hou, J. J.; Wang, F. Y.; Han, N.; Xiu, F.; Yip, S. P.; Fang, M.; Lin, H.; Hung, T. F.; Ho, J. C. Stoichiometric Effect on Electrical, Optical, and Structural Properties of Composition-Tunable $In_xGa_{1-x}As$ Nanowires. *ACS Nano* **2012**, *6*, 9320−9325.
(41) Wang, Z. W.; He, X.; Zhang, X. X.; Alshareef, H. N. Hybrid van der Waals p-n Heterojunctions based on SnO and 2D MoS_2. *Adv. Mater.* **2016**, *28*, 9133−9141.
(42) Mishra, U. K.; Singh, J. *Semiconductor Device Physics and Design*; Springer: Dordrecht, 2008.
(43) Wu, Y.; Yan, X.; Zhang, X.; Ren, X. M. A Monolayer Graphene/GaAs Nanowire Array Schottky Junction Self-Powered Photodetector. *Appl. Phys. Lett.* **2016**, *109*, 183101.
(44) Lee, Y. T.; Jeon, P. J.; Han, J. H.; Ahn, J.; Lee, H. S.; Lim, J. Y.; Choi, W. K.; Song, J. D.; Park, M. C.; Im, S.; Hwang, D. K. Mixed-Dimensional 1D ZnO-2D WSe_2 van der Waals Heterojunction Device for Photosensors. *Adv. Funct. Mater.* **2017**, *27*, 1703822.
(45) Lee, C.; Yan, H.; Brus, L. E.; Heinz, T. F.; Hone, J.; Ryu, S. Anomalous Lattice Vibrations of Single- and Few-Layer MoS_2. *ACS Nano* **2010**, *4*, 2695−2700.
(46) Zhou, X.; Hu, X. Z.; Zhou, S. S.; Song, H. Y.; Zhang, Q.; Pi, L. J.; Li, L.; Li, H. Q.; Lu, J. T.; Zhai, T. Y. Tunneling Diode Based on WSe_2/SnS_2 Heterostructure Incorporating High Detectivity and Responsivity. *Adv. Mater.* **2018**, *30*, 1703286.
(47) Luong, D. H.; Lee, H. S.; Neupane, G. P.; Roy, S.; Ghimire, G.; Lee, J. H.; Vu, Q. A.; Lee, Y. H. Tunneling Photocurrent Assisted by Interlayer Excitons in Staggered van der Waals Hetero-Bilayers. *Adv. Mater.* **2017**, *29*, 1701512.
(48) Jiang, X. X.; Shi, X. Y.; Zhang, M.; Wang, Y. R.; Gu, Z. H.; Chen, L.; Zhu, H.; Zhang, K.; Sun, Q. Q.; Zhang, D. W. A Symmetric Tunnel Field-Effect Transistor Based on MoS_2/Black Phosphorus/MoS_2 Nanolayered Heterostructures. *ACS Appl. Nano Mater.* **2019**, *2*, 5674−5680.
(49) Coehoorn, R.; Haas, C.; Dijkstra, J.; Flipse, C. J. F.; Degroot, R. A.; Wold, A. Electronic-Structure of $MoSe_2$, MoS_2, and WSe_2. I. Band-Structure Calculations and Photoelectron-Spectroscopy. *Phys. Rev. B* **1987**, *35*, 6195−6202.
(50) Coehoorn, R.; Haas, C.; Degroot, R. A. Electronic-Structure of $MoSe_2$, MoS_2, and WSe_2. II. The Nature of the Optical Band Gaps. *Phys. Rev. B* **1987**, *35*, 6203−6206.
(51) Hong, X. P.; Kim, J.; Shi, S. F.; Zhang, Y.; Jin, C. H.; Sun, Y. H.; Tongay, S.; Wu, J. Q.; Zhang, Y. F.; Wang, F. Ultrafast Charge Transfer in Atomically Thin MoS_2/WS_2 Heterostructures. *Nat. Nanotechnol.* **2014**, *9*, 682−686.
(52) Zhang, K. A.; Zhang, T. N.; Cheng, G. H.; Li, T. X.; Wang, S. X.; Wei, W.; Zhou, X. H.; Yu, W. W.; Sun, Y.; Wang, P.; Zhang, D.; Zeng, C. G.; Wang, X. J.; Hu, W. D.; Fan, H. J.; Shen, G. Z.; Chen, X.; Duan, X. F.; Chang, K.; Dai, N. Interlayer Transition and Infrared Photodetection in Atomically Thin Type-II $MoTe_2$/MoS_2 van der Waals Heterostructures. *ACS Nano* **2016**, *10*, 3852−3858.
(53) Prasai, D.; Klots, A. R.; Newaz, A. K. M.; Niezgoda, J. S.; Orfield, N. J.; Escobar, C. A.; Wynn, A.; Efimov, A.; Jennings, G. K.; Rosenthal, S. J.; Bolotin, K. I. Electrical Control of Near-Field Energy

https://doi.org/10.1021/acsnano.2c03673
ACS Nano XXXX, XXX, XXX−XXX

Transfer between Quantum Dots and Two-Dimensional Semiconductors. *Nano Lett.* **2015**, *15*, 4374−4380.
(54) Chen, K.; Wan, X.; Wen, J. X.; Xie, W. G.; Kang, Z. W.; Zeng, X. L.; Chen, H. J.; Xu, J. B. Electronic Properties of MoS_2-WS_2 Heterostructures Synthesized with Two-Step Lateral Epitaxial Strategy. *ACS Nano* **2015**, *9*, 9868−9876.
(55) Zhou, J. Y.; Xie, M. Z.; Ji, H.; Cui, A. Y.; Ye, Y.; Jiang, K.; Shang, L. Y.; Zhang, J. Z.; Hu, Z. G.; Chu, J. H. Mixed-Dimensional van der Waals Heterostructure Photodetector. *ACS Appl. Mater. Inter.* **2020**, *12*, 18674−18682.
(56) Santos, E. J. G.; Kaxiras, E. Electrically Driven Tuning of the Dielectric Constant in MoS_2 Layers. *ACS Nano* **2013**, *7*, 10741−10746.
(57) Neidert, R. E. Dielectric-Constant of Semi-Insulating Gallium Arsenide. *Electron. Lett.* **1980**, *16*, 244−245.
(58) Hayne, M.; Maes, J.; Bersier, S.; Moshchalkov, V. V.; Schliwa, A.; Muller-Kirsch, L.; Kapteyn, C.; Heitz, R.; Bimberg, D. Electron Localization by Self-Assembled GaSb/GaAs Quantum Dots. *Appl. Phys. Lett.* **2003**, *82*, 4355−4357.
(59) Choi, W.; Cho, M. Y.; Konar, A.; Lee, J. H.; Cha, G. B.; Hong, S. C.; Kim, S.; Kim, J.; Jena, D.; Joo, J.; Kim, S. High-Detectivity Multilayer MoS_2 Phototransistors with Spectral Response from Ultraviolet to Infrared. *Adv. Mater.* **2012**, *24*, 5832−5836.
(60) Liu, X.; Gu, L. L.; Zhang, Q. P.; Wu, J. Y.; Long, Y. Z.; Fan, Z. Y. All-Printable Band-Edge Modulated ZnO Nanowire Photodetectors with Ultra-High Detectivity. *Nat. Commun.* **2014**, *5*, 4007.
(61) Yin, J. B.; Tan, Z. J.; Hong, H.; Wu, J. X.; Yuan, H. T.; Liu, Y. J.; Chen, C.; Tan, C. W.; Yao, F. R.; Li, T. R.; Chen, Y. L.; Liu, Z. F.; Liu, K. H.; Peng, H. L. Ultrafast and Highly Sensitive Infrared Photodetectors Based on Two-Dimensional Oxyselenide Crystals. *Nat. Commun.* **2018**, *9*, 3311.
(62) Zhang, H. B.; Zhang, X. J.; Liu, C.; Lee, S. T.; Jie, J. S. High-Responsivity, High-Detectivity, Ultrafast Topological Insulator Bi_2Se_3/Silicon Heterostructure Broadband Photodetectors. *ACS Nano* **2016**, *10*, 5113−5122.
(63) Yang, T. F.; Zheng, B. Y.; Wang, Z.; Xu, T.; Pan, C.; Zou, J.; Zhang, X. H.; Qi, Z. Y.; Liu, H. J.; Feng, Y. X.; Hu, W. D.; Miao, F.; Sun, L. T.; Duan, X. F.; Pan, A. L. Van der Waals Epitaxial Growth and Optoelectronics of Large-Scale WSe_2/SnS_2 Vertical Bilayer p-n Junctions. *Nat. Commun.* **2017**, *8*, 1906.
(64) Luo, T.; Liang, B.; Liu, Z.; Xie, X. M.; Lou, Z.; Shen, G. Z. Single-GaSb-Nanowire-Based Room Temperature Photodetectors with Broad Spectral Response. *Sci. Bull.* **2015**, *60*, 101−108.
(65) Liao, F. Y.; Deng, J. N.; Chen, X. Y.; Wang, Y.; Zhang, X. Z.; Liu, J.; Zhu, H.; Chen, L.; Sun, Q. Q.; Hu, W. D.; Wang, J. L.; Zhou, J.; Zhou, P.; Zhang, D. W.; Wan, J.; Bao, W. Z. A Dual-Gate MoS_2 Photodetector Based on Interface Coupling Effect. *Small* **2020**, *16*, 1904369.
(66) Sun, G. Z.; Li, B.; Li, J.; Zhang, Z. W.; Ma, H. F.; Chen, P.; Zhao, B.; Wu, R. X.; Dang, W. Q.; Yang, X. D.; Tang, X. W.; Dai, C.; Huang, Z. W.; Liu, Y.; Duan, X. D.; Duan, X. F. Direct van der Waals Epitaxial Growth of 1D/2D Sb_2Se_3/WS_2 Mixed-Dimensional p-n Heterojunctions. *Nano Res.* **2019**, *12*, 1139−1145.
(67) Tan, C. Y.; Yin, S. Q.; Chen, J. W.; Lu, Y.; Wei, W. S.; Du, H. F.; Liu, K. L.; Wang, F. K.; Zhai, T. Y.; Li, L. Broken-Gap PtS_2/WSe_2 van der Waals Heterojunction with Ultrahigh Reverse Rectification and Fast Photoresponse. *ACS Nano* **2021**, *15*, 8328−8337.
(68) Islam, A.; Lee, J.; Feng, P. X. L. Atomic Layer GaSe/MoS_2 van der Waals Heterostructure Photodiodes with Low Noise and Large Dynamic Range. *ACS Photonics* **2018**, *5*, 2693−2700.
(69) Wu, F.; Xia, H.; Sun, H. D.; Zhang, J. W.; Gong, F.; Wang, Z.; Chen, L.; Wang, P.; Long, M. S.; Wu, X.; Wang, J. L.; Ren, W. C.; Chen, X. S.; Lu, W.; Hu, W. D. AsP/InSe Van der Waals Tunneling Heterojunctions with Ultrahigh Reverse Rectification Ratio and High Photosensitivity. *Adv. Funct. Mater.* **2019**, *29*, 1900314.
(70) Kim, C. O.; Kim, S.; Shin, D. H.; Kang, S. S.; Kim, J. M.; Jang, C. W.; Joo, S. S.; Lee, J. S.; Kim, J. H.; Choi, S. H.; Hwang, E. High Photoresponsivity in an All-Graphene p-n Vertical Junction Photodetector. *Nat. Commun.* **2014**, *5*, 3249.
(71) Wang, P.; Liu, S. S.; Luo, W. J.; Fang, H. H.; Gong, F.; Guo, N.; Chen, Z. G.; Zou, J.; Huang, Y.; Zhou, X. H.; Wang, J. L.; Chen, X. S.; Lu, W.; Xiu, F. X.; Hu, W. D. Arrayed van der Waals Broadband Detectors for Dual-Band Detection. *Adv. Mater.* **2017**, *29*, 1604439.
(72) Snaith, H. J.; Schmidt-Mende, L.; Gratzel, M.; Chiesa, M. Light Intensity, Temperature, and Thickness Dependence of the Open-Circuit Voltage in Solid-State Dye-Sensitized Solar Cells. *Phys. Rev. B* **2006**, *74*, 045306.
(73) Furchi, M. M.; Holler, F.; Dobusch, L.; Polyushkin, D. K.; Schuler, S.; Mueller, T. Device Physics of van der Waals Heterojunction Solar Cells. *Npj. 2d Mater. Appl.* **2018**, *2*, 3.
(74) Klee, V.; Preciado, E.; Barroso, D.; Nguyen, A. E.; Lee, C.; Erickson, K. J.; Triplett, M.; Davis, B.; Lu, I. H.; Bobek, S.; McKinley, J.; Martinez, J. P.; Mann, J.; Talin, A. A.; Bartels, L.; Leonard, F. Superlinear Composition-Dependent Photocurrent in CVD-Grown Monolayer $MoS_{2(1-x)}Se_{2x}$ Alloy Devices. *Nano Lett.* **2015**, *15*, 2612−2619.
(75) Li, L.; Wang, W. K.; Gan, L.; Zhou, N.; Zhu, X. D.; Zhang, Q.; Li, H. Q.; Tian, M. L.; Zhai, T. Y. Ternary Ta_2NiSe_5 Flakes for a High-Performance Infrared Photodetector. *Adv. Funct. Mater.* **2016**, *26*, 8281−8289.

https://doi.org/10.1021/acsnano.2c03673
ACS Nano XXXX, XXX, XXX−XXX